

Origin of an unintended increase in carrier density of ternary cation-based amorphous oxide  
semiconductors

Mingyuan Liu<sup>1</sup>, Xingyu Wang<sup>1</sup>, Han Wook Song<sup>2</sup>, Hyeonghun Kim<sup>1</sup>, Michael Clevenger<sup>1</sup>,  
Dong-Kyun Ko<sup>3</sup>, Kwangsoo No<sup>4</sup>, and Sunghwan Lee<sup>1\*</sup>

<sup>1</sup> School of Engineering Technology, Purdue University, West Lafayette, IN 47907, USA

<sup>2</sup> Center for Mass and Related Quantities, Korea Research Institute of Standard and Science,  
Daejeon 34113, South Korea

<sup>3</sup> Department of Electrical and Computer Engineering, New Jersey Institute of Technology,  
Newark, NJ 07102, USA

<sup>4</sup> Department of Materials Science and Engineering, KAIST, Daejeon 34141, South Korea

Keywords: amorphous oxide semiconductors; work function; carrier density; thin film  
transistors; indium oxides; InAlZnO

\*Corresponding authors: [sunghlee@purdue.edu](mailto:sunghlee@purdue.edu)

## Abstract

In thin film transistors (TFTs), carrier density in the channel layer is a fundamental intrinsic factor to engineer desirable TFT performance parameters such as the threshold voltage, drain current, and on-to-off ratio. Here, we report on the origin of carrier density modulation in a ternary cation system of InAlZnO (IAZO) and its effect on the TFT performance. Through work function investigations and bandgap analysis, the carrier density of IAZO is found to be increased by  $> 10^4$  times compared to that of unannealed IAZO after low temperature annealing at 200 °C in air. Photoelectron spectroscopic studies reveal that the typical intrinsic (vacancy-based native defect) or extrinsic (cation substitution) doping mechanisms are not the primary cause of the channel carrier increase. From high pressure oxidation with much enhanced reactivity of reaction gases, it is identified that the equilibrium carrier density of IAZO is much higher than those used in typical TFT channel application. The low channel carrier density tends to increase and reach the higher equilibrium carrier density in the absence of kinetic constraints. The combinatorial investigations presented herein help understand the origin of unintentional increase in channel carrier density in amorphous oxides and its effect on the operation of TFTs.

## 1. Introduction

Metal oxides have attracted much attention for applications in next generation electronic and optoelectronic devices such as fast-switching high resolution displays<sup>1-2</sup>, photovoltaics<sup>3</sup> and sensors<sup>4-5</sup> due to their tunable electrical conductivity<sup>6</sup>, high optical transparency in the visible range<sup>7</sup>, and high carrier mobility<sup>8</sup>. More recently, amorphous oxide semiconductors (AOSs) with the electronic configuration,  $(n-1)d^{10}ns^0$  ( $n \geq 5$ ) have emerged as a promising candidate for thin film transistor (TFT) channel application<sup>9-10</sup>. The large, spatially-extended hybridized metal  $ns$  orbitals directly overlap with neighboring orbitals to ensure favorable carrier transport paths<sup>1</sup> and hence, lead to much higher carrier mobility despite in its amorphous state consisting of metal-oxygen-metal chemical bond disorders. Its mobility has been widely reported to be an order of magnitude higher than the conventional amorphous Si counterpart ( $< \sim 1 \text{ cm}^2/\text{Vs}$ ). Furthermore, these amorphous semiconductors can be deposited using low temperature processing methods<sup>1, 11</sup> with large area uniformity, which brings about a significant reduction in the manufacturing cost. In addition, the low temperature processing enables ones to implement heat sensitive polymeric or fabric substrates for potential flexible and wearable device applications.

There have been considerable efforts to incorporate this class of materials into devices, particularly in current-driven active matrix displays such as organic light emitting diode displays as pixel-driving switching elements. Strategies to enhance amorphous phase stability, reduce bias stress-induced threshold voltage shifts, and suppress channel carrier densities have been studied and successfully applied to the switching TFT application. Third cation elements are often added to binary cation oxide systems to limit the channel carrier generation for TFT channel application. We have recently reported that the addition of Al to InZnO, a typical binary cation

material system leads to enhanced amorphous phase stability, carrier suppression capability and higher carrier mobility, up to  $\sim 45 \text{ cm}^2/\text{Vs}$  (Hall Effect mobility) and  $\sim 20 \text{ cm}^2/\text{Vs}$  (field effect mobility)<sup>12</sup>. All of these characteristics are expected to be a key enabler for realizing the next generation ultra-high-definition displays.

Post-process annealing is widely employed in AOS-based TFT fabrication since annealing has been shown to improve field effect mobility<sup>13-14</sup> and channel/metallization contacts<sup>11, 15</sup> as well as reduce trap density<sup>16</sup>, which often leads to unstable device performance or unfavorable hysteresis in their transistor characteristics<sup>16-17</sup>. It has been reported that post-annealing at temperatures ranging from 100 °C to 400 °C in air increased TFT field effect mobility from 5-10 to 15  $\text{cm}^2/\text{Vs}$  for ternary cation AOS of IGZO channel and 10-20 to 25-30  $\text{cm}^2/\text{Vs}$  for binary cation, IZO channel. However, the post-annealing is often accompanied by an increase in channel carrier density that induces an unfavorable increase in the device off-state current and operation voltages<sup>2, 13</sup>. Nomura *et al.*<sup>18</sup> previously reported that post-annealing at 400 °C improves IGZO TFT stability but they also found that thermal annealing results in up to  $\sim -7 \text{ V}$  threshold voltage shift. Kikuchi *et al.*<sup>19</sup> also reported on the threshold voltage instability of IGZO TFTs up to  $\sim -48 \text{ V}$  after dry and wet annealing at 150–400 °C. Barquinha *et al.*<sup>20</sup> and Lee *et al.*<sup>14</sup> studying IZO TFTs reported a large negative threshold voltage shift of  $\sim -13-15 \text{ V}$  after annealing at 125-200 °C. To date, the origin of the increase in channel carrier density after annealing has not been fully understood. Some studies reported that changes in carrier density and hence conductivity after annealing were mainly attributed to the oxygen vacancy-based carrier generation/annihilation mechanism<sup>21-22</sup>. However, studies are also found in the literature that show an increase in carrier density after annealing in the presence of O<sub>2</sub>, for which the

oxygen-vacancy mechanism is not responsible for the carrier density increase. In a density function study, Kamiya *et al.*<sup>23-24</sup> reported a mechanism that suggests a transition in defect state within the bandgap from deep levels to shallow levels after annealing, which was further validated by Yeon *et al.*<sup>25</sup> through the physical identification of change in defect states.

The current study aims to identify the origin of an increase in carrier density after low-temperature annealing conducted in air, particularly for a third-cation AOS system of InAlZnO (IAZO). The performance of amorphous IAZO-based TFTs is first compared before and after annealing. Changes in Fermi level energy and bandgap are then investigated using photoelectron spectroscopy and UV-Vis analysis to analyze the change in their electronic structure. Lastly, a high pressure oxidation experiment is conducted for the equilibrium carrier density analysis. The equilibrium carrier density results are compared with the defect state transition mechanism to account for a significant increase in carrier density of IAZO after low-temperature annealing.

## **2. Experimental details**

A ternary cation AOS of IAZO films (In:Al:Zn = 66.6:8.9:2.1 in wt.% ratio) were deposited on Si and glass substrates using co-sputtering of ceramic InZnO (IZO) and metal Al targets. Substrates were sequentially cleaned with acetone, isopropyl alcohol and de-ionized water in order to remove any potential contamination on the surface, and then loaded into the sputter chamber. After achieving a base pressure of  $< 6 \times 10^{-7}$  Torr for the main chamber, IAZO films were deposited at an Ar/O<sub>2</sub> gas volume fraction of 80/20 and a working pressure of  $2 \times 10^{-3}$  Torr. Prior to film depositions, pre-sputtering was performed for 5-10 mins to clean out any surface contaminants on the target surface and ensure uniform gas flow and chamber pressure.

Ternary-cation IAZO-based TFTs were fabricated in a bottom-gated configuration with a channel IAZO thickness of 30 nm. Heavily-doped Si ( $0.003\text{-}0.005\ \Omega\text{cm}$ ) was used as the bottom gate electrode and substrate with thermally grown SiO<sub>2</sub> (50 nm thick) as the gate dielectric. For the source and drain metallization, Al was sputtered to a thickness of 100 nm at a pure Ar atmosphere and the same working pressure of  $2\times 10^{-3}$  Torr for channel IAZO. All depositions for channel and metallization layers were conducted at room temperature. To define channel and metallization regions, *in-situ* shadow masks were used. Device output and transfer characteristics were evaluated with a semiconductor parameter analyzer (Agilent 4155B) in a light-tight probe station under ambient conditions.

For the evaluations of optoelectronic properties, UV-Vis measurements were made on IAZO films grown on glass substrates in wavelengths ranging from 300 to 900 nm through a Varian Cary 50 spectrometer. Bare glass was used as a reference baseline to exclude the substrate effect on the resulting transmittance/absorption spectra. From Tauc plots, the optical bandgap of IAZO was estimated for direct band-to-band transitions before and after annealing. Film thicknesses were measured using a multi-wavelength ellipsometer (FilmSense FS-1) with an incident and detection angle of 65°. X-ray diffraction (XRD) was utilized to investigate the amorphous/crystalline structure of IAZO films deposited on glass substrates before and after annealing in a Bruker D5000 diffractometer at 40 kV and 40 mA with Cu K $\alpha$  radiation ( $\lambda=1.54\ \text{\AA}$ ). In order to maximize the diffraction intensity from IAZO thin films, glancing incident angle XRD measurements were conducted with an incident angle of approximately 1°.

The valence states and chemical environments of major elements of IAZO and work function were determined by x-ray photoelectron spectroscopy (XPS) in a Thermo Scientific K-Alpha XPS spectrometer with focused monochromatic soft Al K $\alpha$  X-ray radiation at 1486.6 eV. All the measurements were performed under ultra high vacuum at a pressure below  $2 \times 10^{-8}$  Torr. A low energy electron flood gun was employed to remove accumulated charges and neutralize the sample surface during the measurements. Prior to XPS measurements, the sample surface was cleaned by Ar cluster ions ( $\text{Ar}_n^+$ ) to remove any surface contaminants, of which the cluster ion source was used to limit any chemical damages such as reduction of the oxide due to, known as, preferential sputtering. The cluster ion cleaning was performed at an ion beam energy of 4 keV, a cluster size  $n$  of 1000, and a cluster energy per nucleon  $\varepsilon$  of 4 eV/nucleon for 20 sec. Multi-channel electron detection lenses were located at an angle of  $55^\circ$  from the surface normal to collect emitted photoelectrons. During work function measurements, the IAZO films were negatively biased with respect to earth ( $V_{bias} = -30$  V) by the conducting sample stage, through which the emitted electrons are accelerated and hence the onset of emission is detected. Before the measurements, gold specimen was used as reference to calibrate the spectrometer and the binding energy scale, which allows accurate determinations of onset energy and Fermi level position.

For equilibrium carrier density analysis, the as-deposited IAZO films were oxidized at pressures ranging from 200-800 atm and temperatures of 200-450 °C with ultra high purity (UHP, >99.99%) dry oxygen. More detailed experimental procedures can be found elsewhere<sup>26-27</sup>.

Briefly, the samples were loaded into a quartz lined high pressure vessel surrounded by the furnace chamber. Over the course of high pressure annealing, temperature was maintained within approximately  $\pm 5$  °C by monitoring double thermocouples attached to the outside of the reactor,

and pressure was kept within  $\pm 10$  atm by monitoring a pressure gauge connected to the pressure vessel. High pressure reaction was terminated after 15 hours by moving the furnace away from the reactor tube. After the reactor and contents had cooled down to  $< \sim 70$  °C, the chamber was vented, and the samples were removed.

### 3. Results and discussion

Amorphous IAZO TFTs were fabricated and the performance was compared before and after annealing in air at 200 °C for one hour. The amorphous structure of IAZO was maintained after annealing as shown in the XRD spectra in Figure S1. Output characteristics of unannealed IAZO TFTs that evaluate drain current ( $I_D$ ) as a function of drain bias ( $V_D$ , primary) and gate bias ( $V_G$ , secondary) are shown in **Figure 1(a)**. Clear drain current saturation behaviors are observed for the output curves without any current crowding, particularly at the low  $V_D$  regime ( $V_D < \sim 1$  V), which indicates that Ohmic contacts are formed at the channel/metallization interface. After annealing, output characteristics exhibit higher drain current at the same applied gate voltages compared to that of unannealed IAZO TFTs (*e.g.*, at  $V_G = 10$  V,  $\sim 1.7 \times 10^{-5}$  A vs.  $1 \times 10^{-3}$  A for as-fabricated and annealed devices, respectively), as shown in Figure 1(b).

Transfer characteristics were investigated in the saturation regime by scanning the gate bias at a fixed drain bias of  $V_D = 20$  V, which was selected from the output characteristics in Figure 1(a,b) to ensure that the devices were well into the saturation regime of drain current. In Figure 1(c), the device drain current on/off ratio is determined to be greater than  $10^7$  for both as-fabricated and annealed TFTs from the plots of  $I_D$  vs.  $V_G$  where the off-state is selected for the lowest current and the on-state is chosen for the highest current measured. The field effect mobility and

the threshold voltage are estimated from the  $(I_D)^{1/2}$ - $V_G$  plots shown in Figure 1(d), from the slope and the x-axis intercept of the linear extrapolation, respectively. For as-fabricated TFTs, the saturation field effect mobility is  $7.64 \text{ cm}^2/\text{Vs}$  and the threshold voltage is found to be approximately  $7.49 \text{ V}$ . After annealing the saturation mobility is significantly enhanced to  $\sim 21.72 \text{ cm}^2/\text{Vs}$ , which is more than 3-6 times higher than other ternary cation-based amorphous oxide TFTs, such as InGaZnO-based TFTs,<sup>1, 19, 28</sup> and comparable to binary oxide InZnO-TFTs<sup>29-30</sup>. The threshold voltage significantly shifts from  $7.49 \text{ V}$  (before annealing) to  $-1.81 \text{ V}$  (after annealing), which is beneficial for minimizing stand-by power consumption as it is located closer to the zero bias. It is important to identify the origins that lead to a large change in the threshold voltage between the as-fabricated and annealed devices, which will be further discussed with the work function measurements and trap density estimations.

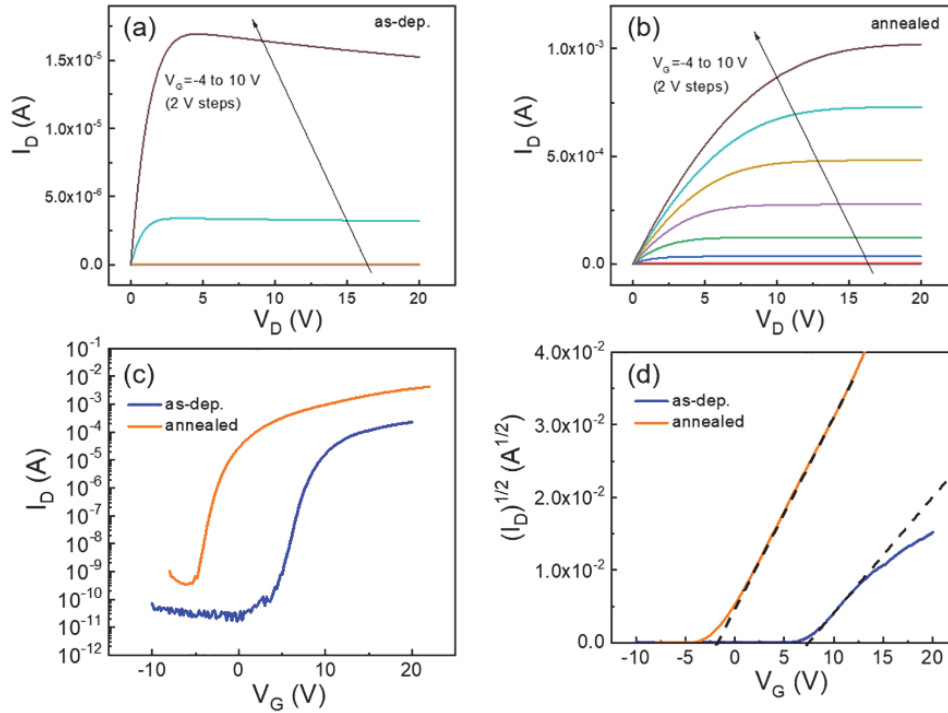


**Figure 1.** IAZO-based TFT performance: output characteristics of (a) as-deposited and (b)  $200^\circ\text{C}$ -annealed devices; and transfer characteristics of (c)  $I_D$ - $V_G$  and (d)  $(I_D)^{1/2}$ - $V_G$  curves, from which the as-deposited and annealed TFTs show good  $I_D$  saturation behavior, on/off ratio of

$\sim 10^7$ . The saturation field effect mobility was enhanced after annealing from 7.64 to 21.72  $\text{cm}^2/\text{Vs}$  and the threshold voltage shifts from relatively large 7.49 to -1.81 V.

To better understand the changes in the TFT behaviors before and after annealing, we have investigated the carrier density between the as-deposited and annealed cases. Due to the resistive nature of thin and low carrier density materials such as TFT channel layers, consistent and reliable Hall Effect measurements are often limited due to the low applied currents to prevent sample joule heating. In the present study, instead, the work function of IAZO films was evaluated using photoelectron spectroscopy to investigate changes in carrier density before and after annealing. The position of the Fermi level ( $E_F$ ) and the onset cut-off kinetic energy ( $E_{onset}$ ), which is the energy of free electrons generated by the photoelectric effect, were measured. The work function ( $\Phi$ ) was then determined by the equation below with the photon energy ( $h\nu=1486.6$  eV in this study):

$$E_{onset} = (E_F + \Phi) - h\nu \quad (1)$$

**Figure 2(a)** shows the measurement results obtained from as-deposited IAZO where the  $E_{onset}$  energy of 33.31 eV is estimated using linear extrapolation. **Figure 2(b)** shows the position of  $E_F$  obtained from as-deposited IAZO, which is found to be  $\sim 1515.14$  eV. From these values, the work function is estimated to be 4.77 eV. Similarly, the work function of annealed IAZO is determined to be 4.53 eV from **Figure 2(c,d)**, which is 0.24 eV lower than that of as-deposited IAZO. This suggests that Fermi level shifts toward the conduction band ( $E_C$ ) and the electron carrier density increased after annealing. From the measured work function of IAZO, it is further confirmed that Ohmic contacts were created at the channel/metallization interface for both as-

deposited and annealed TFTs since the work function of Al is reported as 4.1-4.2 eV and Ohmic contacts are formed when the metal work function is smaller than that of n-type semiconductors.

The carrier density ( $n$ ) for n-type semiconductors is related with the effective conduction band density of states ( $N_C$ ), Boltzmann constant ( $k_B$ ), temperature ( $T$ ) in Kelvin,  $E_F$  and  $E_C$  in the equation below:

$$n = N_C \exp\left(\frac{E_F - E_C}{k_B T}\right) \quad (2)$$

From the equation above, the ratio between the carrier densities before and after annealing ( $n_{ch,anneal}/n_{ch,asdep}$ ) is approximated to the change in  $E_F$ , which is equivalent to the change in work function when the band energy structures remain nearly the same after annealing. According to UV-Vis measurements before and after annealing, it is confirmed that no significant changes are observed in absorption spectra and the bandgap values are nearly identical as 3.25-3.31 eV for both as-deposited and annealed IAZO. The UV-Vis results will be further discussed later with Figure 3. Then, from the work function difference ( $\Delta\Phi=0.24$  eV) and the relation,  $\exp(\Delta\Phi/k_B T)$  at room temperature, the carrier density after annealing is determine to be 10,729 times higher than that of as-deposited IAZO (i.e.,  $n_{ch,anneal}/n_{ch,asdep}=10,729$ ).

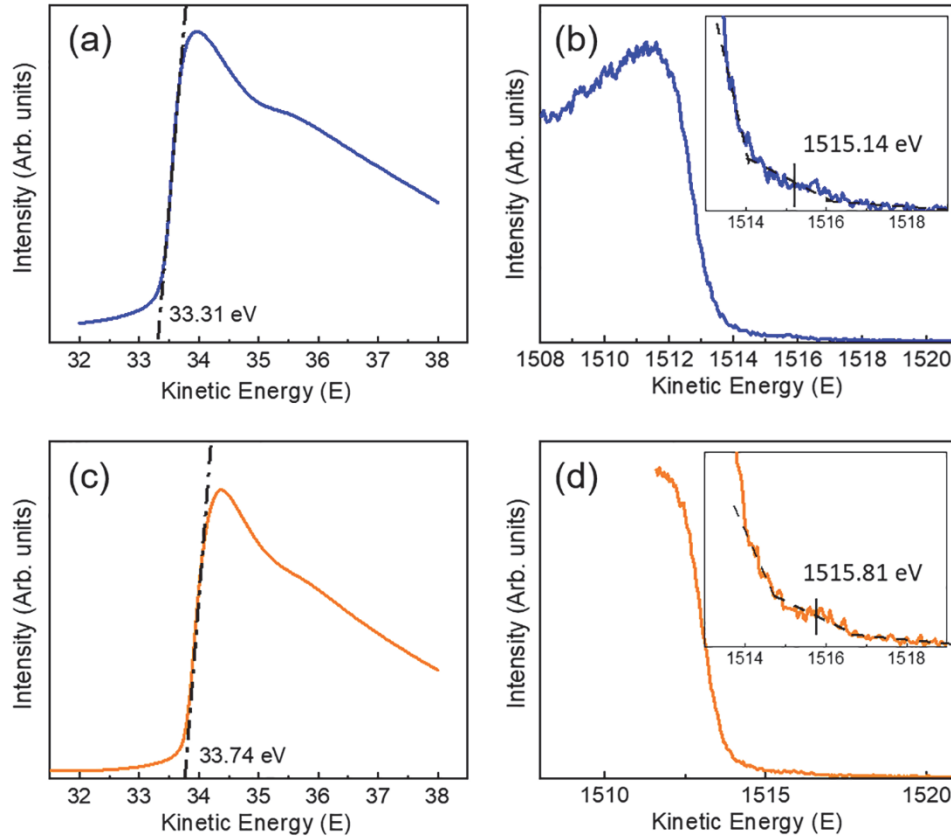


**Figure 2.** Work function measurements through photoelectron microscopy: the work function of the as-deposited and annealed IAZO was evaluated from onset cut-off energy and Fermi energy measurements on (a,b) as-deposited and (c,d) annealed IAZO films, respectively where the work functions were determined to be 4.77 eV for as-deposited IAZO and 4.53 eV for annealed IAZO, indicating the  $E_F$  moves toward to the conduction band due to an increase in carrier density.

To evaluate the effect of the increased carrier density on the optoelectronic properties of IAZO before and after annealing, UV-Vis measurements were conducted. **Figure 3(a)** shows visible regime transparency of IAZO at wavelengths ranging from 300 to 900 nm. Although the transparency of annealed IAZO slightly increases, overall high visible-regime transmittance was achieved (>90%) for both the as-deposited and annealed states and no significant differences were observed before and after annealing. Tauc plots of  $(\alpha h\nu)^2$  vs.  $h\nu$  for the direct bandgap transition are presented in Figure 3(b), from which the optical bandgap of IAZO is compared before and after annealing. As expected from the nearly identical transmittance curves in Figure

3(a), the Tauc plots are also similar to each other and the extracted bandgap of annealed samples is only slightly increased by  $\sim 0.06$  eV from 3.25 eV (as-deposited) to 3.31 eV (annealed), in spite of the abrupt increase in carrier density, more than  $10^4$  times compared to that of as-deposited IAZO.

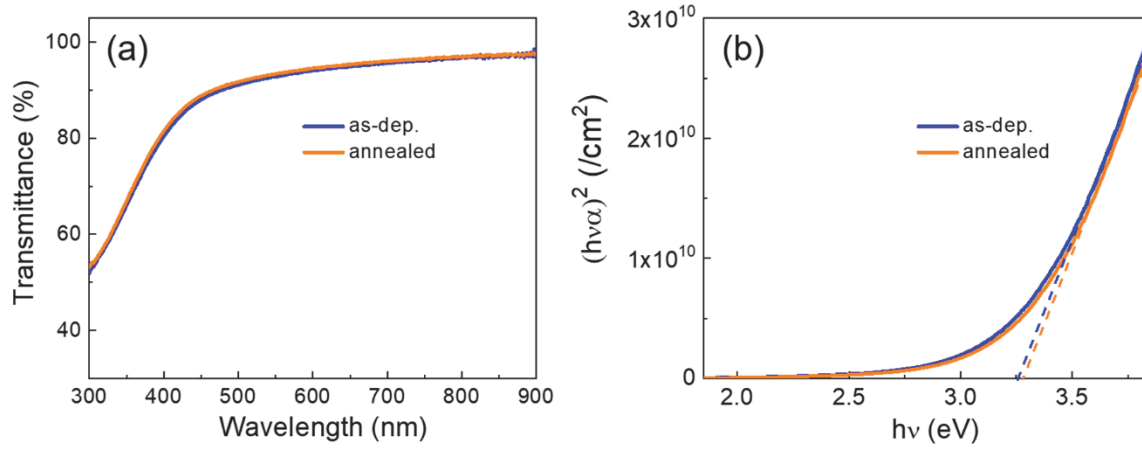


**Figure 3.** UV-Vis investigations of (a) transmittance in the visible regime, which exhibits high visible transparency ( $>90\%$ ) for both IAZO films before and after annealing; and (b) Tauc plot for the direct bandgap transition, from which the optical bandgap of IAZO is estimated to be  $\sim 3.25$  eV for as-deposited state and  $\sim 3.31$  eV for annealed state.

One may be curious if the Burstein-Moss (BM) theory that explains an increase in optical bandgap when excess valence electrons are excited to the conduction band (i.e., band-to-band transition) accounts for the behavior, shown in this study, of the significant increase in carrier density ( $>10^4$  times) without noticeable changes in bandgap. The BM shift of  $E_G$  is expressed by the following equation, relating the carrier density ( $n$ ) and the change in bandgap in response to photo excitation with the effective mass,  $m^*$  and the Planck constant  $h$ <sup>7, 31</sup>:

$$\Delta E_G = \left( \frac{h^2}{8m^*} \right) \left( \frac{3n}{\pi} \right)^{2/3} \quad (3)$$

According to the above equation, the theoretical BM shift is shown in **Figure 4** as a function of effective mass and carrier density in IAZO. The plots indicate that no considerable BM shift is

made with (i) decreasing carrier density, particularly below  $10^{19} / \text{cm}^3$  and (ii) increasing effective mass, particularly greater than approximately 0.6. Since the BM shift is not prominent for the carrier density of  $10^{17}$  and  $10^{18} / \text{cm}^3$ , inset shows a magnified scale of the BM shift for the carrier density of  $10^{17}$  and  $10^{18} / \text{cm}^3$ . The effective mass of  $\text{In}_2\text{O}_3$ -based oxide semiconductors has been reported through experimental and theoretical methods, ranging from 0.21 to  $0.56m_e$ <sup>32-34</sup>. Within this range of  $m^*/m_e=0.21$ -0.56, only a slight BM shift (from 0.012 to 0.006 eV) will be expected for the IAZO carrier density on the order of  $10^{18} / \text{cm}^3$  or below, which is well matched with the extracted optical bandgap exhibited in Figure 3 that presents no significant changes in optical  $E_G$ . Therefore, the BM theory still holds for the current work, reporting a noteworthy increase in carrier density ( $>\sim 10^4 / \text{cm}^3$ ) after low temperature annealing without prominent differences in  $E_G$ .

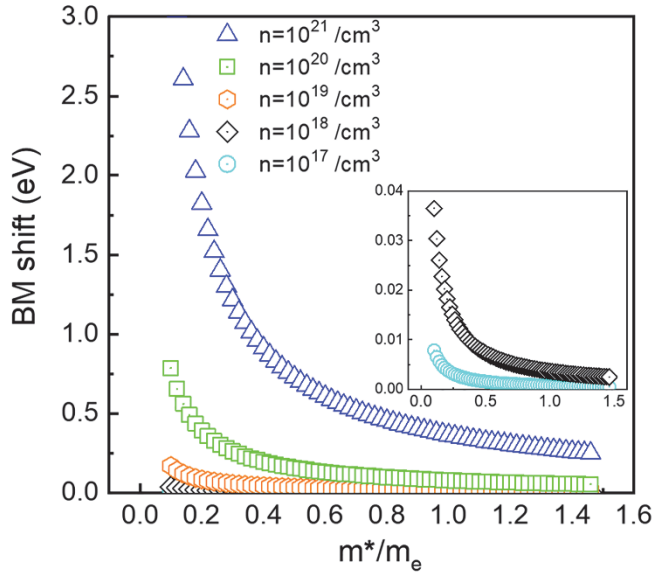


**Figure 4.** Plot of BM shift of  $E_G$  as a function of the ratio of effective mass ( $m^*$ ) over  $m_e$  and carrier density that shows that the BM shift is less significant at the lower carrier density regime below  $n=10^{18} / \text{cm}^3$ , which is the regime of carrier density for typical TFT channel application. An inset shows magnified BM shifts for carrier densities of  $10^{17}$  and  $10^{18} / \text{cm}^3$ .

A change in threshold voltage ( $\Delta V_T$ ) is expressed by, when the change in the sum of the work function difference between the gate and channel, and the energy level difference between  $E_F$  and intrinsic level are negligible:

$$\Delta V_T = \frac{q\Delta(Q_i+Q_d)}{C_{ox}} \quad (4)$$

where,  $Q_i$  is the effective trap density at the channel/dielectric interface,  $Q_d$  is the depletion charge and  $C_{ox}$  is the dielectric capacitance of  $6.903 \times 10^{-8}$  F/cm<sup>2</sup> for 50 nm SiO<sub>2</sub>. The depletion charge is estimated from  $Q_d = n_{ch} \times l_d$  where the maximum depletion depth,  $l_d$ , is approximated by the channel thickness (30 nm). The trap density,  $Q_i$ , is evaluated from the sub-threshold slope ( $S.S$ ) using:

$$Q_i = \left( \frac{q(S.S)\log(e)}{kT} - 1 \right) \frac{C_{ox}}{q} \quad (5)$$

and

$$S.S = \frac{dV_G}{d(\log I_D)} \quad (6)$$

From the equations above, the sub-threshold slope of the as-deposited and annealed IAZO TFTs is determined to be 0.73 and 0.60 V/decade, respectively, from which the trap density,  $Q_i$  is estimated to be  $4.88 \times 10^{12}$  and  $3.95 \times 10^{12}$  /cm<sup>2</sup>, respectively. According to equation (4), a decrease in trap density is in charge of the  $V_T$  shift as much as 2.16 V (to the negative direction) out of total 9.29 V. In addition, the change in channel carrier density ( $\Delta n_{ch} = n_{ch,anneal} - n_{ch,asdep}$ ) after annealing is also estimated from equation (4) with the determined trap densities, which leads to  $\Delta n_{ch} = 1.03 \times 10^{18}$  /cm<sup>3</sup>. From the result of work function analysis,  $n_{ch,anneal}/n_{ch,asdep} = 10,729$  and  $\Delta n_{ch} = 1.03 \times 10^{18}$  /cm<sup>3</sup>, the channel carrier density after annealing ( $n_{ch,anneal}$ ) is estimated to be  $\sim 1 \times 10^{18}$  /cm<sup>3</sup> for the annealed IAZO TFTs due to the  $>10^4$  times difference. Then, the as-deposited carrier density is found to be  $\sim 1 \times 10^{14}$  /cm<sup>3</sup>. The estimated carrier density in the channel IAZO before and after annealing, and other TFT parameters are summarized in **Table 1**.

**Table 1.** Properties of amorphous IAZO TFTs before and annealing at 200 °C in air

	On/off ratio	$\mu_{\text{sat}}$ [cm <sup>2</sup> /Vs]	S [V/decade]	V <sub>Th</sub> [V]	Q <sub>i</sub> [/cm <sup>2</sup> ]	n <sub>ch</sub> [/cm <sup>3</sup> ]
as-dep. TFTs	>10 <sup>7</sup>	7.64	0.73	7.49	4.88×10 <sup>12</sup>	~10 <sup>14</sup>
annealed TFTs	>10 <sup>7</sup>	20.7	0.60	-1.8	3.95×10 <sup>12</sup>	~10 <sup>18</sup>

The identification of origins of the large carrier density increase ( $> \times 10,000$ ) after annealing is crucial to engineer the channel carrier density and achieve the reliable performance of AOS TFTs.

One possibility is that during annealing oxygen coordination or oxygen stoichiometry in IAZO changes. According to the native defect-based doping mechanism that describes that the generation (or annihilation) of a doubly charged oxygen vacancy ( $VO^{**}$ ) from the oxygen sub lattice ( $OO^x$ ) donates (or compensates) two free carriers via the relation:  $OO^x = 1/2O_2 + VO^{**} + 2e'$ . Therefore, the effect of annealing on the valence state of O 1s of IAZO was investigated by performing core-level high resolution (HR) XPS measurements on the as-deposited and annealed IAZO films. **Figure 5** shows obtained O 1s HR spectra with Gaussian fitting and peak deconvolution. In Figure 5(a) of as-deposited oxygen state, peak asymmetry is observed in the core-level O 1s spectrum and the peak is deconvoluted into two peaks centered at  $530.3 \pm 0.1$  eV (stronger peak, denoted as O 1s-a) and  $531.4 \pm 0.1$  eV (weaker peak, denoted as O 1s-b). The stronger peak, O 1s-a located at lower binding energy is attributed to the stoichiometric oxygen (i.e., oxygen sufficient state) in IAZO<sup>7, 35-36</sup> while the weaker peak, O 1s-b at higher binding energy is due to the oxygen deficient states such as O<sup>2-</sup> ions<sup>7, 35-36</sup>, which indicates the presence of oxygen vacancies, known as native doping agents in indium oxide-based semiconductors<sup>37</sup>. This presence of oxygen deficient species provides required semi-conductivity for TFT channel

application. Note that since the surface of all the IAZO films was sputter-etched prior to the XPS measurements, hydroxyl groups adsorbed on the surface of IAZO films are not in charge of the O 1s-b peak. The areal ratio between the two peaks of O 1s-b/O 1s-a is estimated from the HR spectrum, which is found to approximately 44%. After annealing, although the two peaks of core-level oxygen spectra slightly shift to a lower binding energy in Figure 5(b-c), no significant changes are observed for the O 1s spectra and areal ratio between the two peaks even at higher temperature annealing at 300 °C. This similar ratio between the oxygen states indicates that the overall oxygen valence state remains nearly the same after annealing. Therefore, no evidences were found that additional oxygen vacancies were created after the annealing process to increase the channel carrier density.

Jia *et al.*<sup>38</sup> reported a study on defect structures and subgap states of amorphous IGZO through extended x-ray absorption fine-structure measurements (known as EXAFS) and cathodoluminescence (CL) spectroscopic investigations. In their report, the EXAFS analysis identified oxygen deficient states around In and Zn atoms, and the CL investigations revealed no significant changes in defect and subgap states after air annealing at temperatures below 600 °C. The EXAFS and CL investigations support well our findings that the HR XPS analyses before and after annealing verify the presence of oxygen deficient states in all the IAZO films (as-dep., 200 °C-annealed, and 300 °C-annealed), which is required for n-type conduction for the channel; yet no evidences are found for changes in oxygen deficient or other defect states after annealing (i.e., no changes observed in the valence state of the major elements of In, Al, Zn, and O from core-level HR XPS investigations in Figure 5 and S2).

Unintentional hydrogen (H<sup>+</sup>) doping in the In<sub>2</sub>O<sub>3</sub> structure (both crystalline and amorphous) was suggested through first principles calculations of defect levels in In<sub>2</sub>O<sub>3</sub> using density functional

theory<sup>39-40</sup>. However, the origin of H<sup>+</sup> source has not been established and direct experimental evidence supporting the unintentional H<sup>+</sup> doping is not available in the literature. According to this H<sup>+</sup> doping mechanism, the peak at approximately 531.4 eV is attributed to the H<sup>+</sup> doping. However, since no notable changes are seen in the peak and areal density, H<sup>+</sup> doping, although the mechanism is still arguable, is neither in charge of the carrier density increase after annealing.

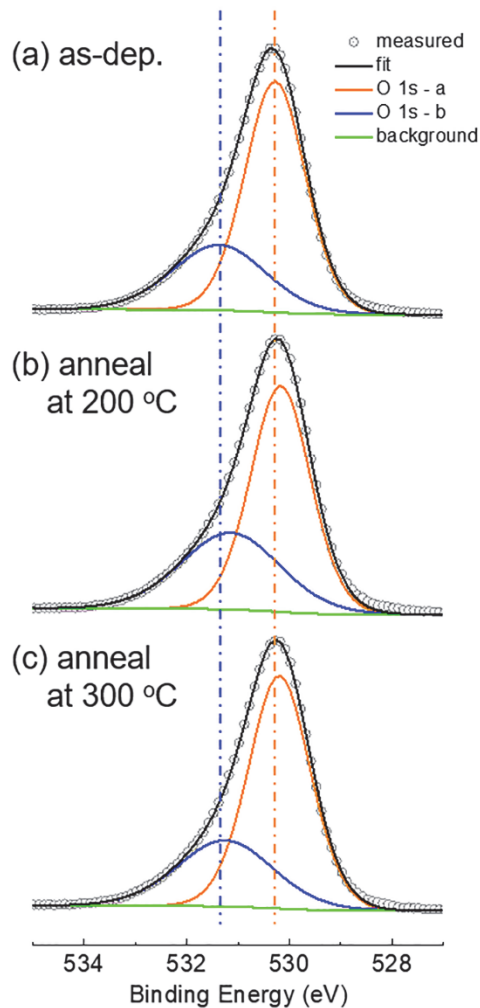
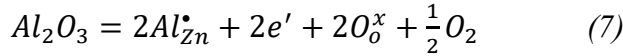


**Figure 5.** Core level HR XPS spectra of O 1s peak deconvoluted into O 1s-a and -b, which representing stoichiometric oxygen and oxygen deficient states, respectively as a function of annealing temperature of (a) as-deposited (not-anneal), (b) 200 °C-annealed and (c) 300 °C-annealed IAZO. No significant changes are observed in the oxygen valence state before and after annealing.

Extrinsic doping is another possibility for the increase in carrier density after annealing.

Although the doped cations of Zn and Al are not activated in amorphous In<sub>2</sub>O<sub>3</sub> as dopants<sup>12, 34</sup>, the substitution of Zn with Al may increase the carrier density since the Al substitution on a Zn sublattice ( $Al_{Zn}^*$ ) donates free electrons to hold charge neutrality, which is the governing impurity doping mechanism in ZnO doped with Al by the relation<sup>41-42</sup>:



During the annealing process, if the energy required for the substitution reaction is provided, additional charge carriers may be created. In this scenario, the valence state of associated cations changes due to the alteration of local coordination by oxygen and coulomb interactions with other nearby elements, which is typically identifiable through photoelectron spectroscopy. To investigate the substitution effect on the carrier generation, core-level HR XPS measurements were made on the major cation elements in IAZO (i.e., In, Al, and Zn). In **Figure S2** of HR XPS spectra for the major elements, no significant changes are detected for all the elements.

Therefore, the cation substitution effect due to the annealing at 200 °C is determined not to be responsible for the observed carrier increase after annealing.

Finally, the equilibrium carrier density of IAZO is considered for the charge of the increase in carrier density after low temperature annealing at 200 °C. We previously reported, through high pressure oxidation investigations and equilibrium constant analysis, that the equilibrium carrier density of amorphous InZnO (IZO), a representative binary cation AOS, is much higher, in its thermodynamic equilibrium state, than that used in typical TFT channel application. Since the class of amorphous oxide semiconductors is based on a thermodynamically metastable phase, when thermodynamic driving forces are provided, the metastable phase tends to transform to a

more stable state, depending on the magnitude of the provided thermodynamic conditions and kinetic constraints. Given high enough thermodynamic conditions and in the absence of kinetic constraints, the amorphous phase of indium oxide-based AOSs undergoes an amorphous-to-crystalline phase transformation as found in the literature (e.g., annealing at temperatures higher than 500 °C in air for 1 hour)<sup>10, 43</sup>. However, at a low annealing temperature, due to limited thermodynamic driving forces and kinetic restraints, only local transformed phases can be achieved in a very short range, which is often defined as local amorphous structure relaxation. In our previous report on *in-situ* resistivity measurements of indium oxide-based AOSs, it has been revealed that two mechanisms of oxygen vacancy-dependent carrier generation/annihilation and amorphous relaxation compete for the overall conduction in amorphous oxides during low temperature annealing where the oxygen vacancy-based mechanism is more rapid process and governs the earlier period of the annealing while the structure relaxation is slow in reaction and more dominant at a later part of annealing<sup>43</sup>.

Similar analyses were made on IAZO to estimate the equilibrium carrier density at an oxygen partial pressure of 0.2 atm, which is the nearly identical oxygen partial pressure in air. **Figure 6** displays the calculated equilibrium density of IAZO at  $P(O_2)=0.2$  atm and compares the IAZO equilibrium carrier density with that of a binary cation AOS of IZO as a function of temperature. The equilibrium carrier density in IAZO is lower than that of IZO at all temperatures, however, much higher than the typical carrier density regime for TFT channel application,  $<\sim 10^{17}-10^{18}$  /cm<sup>3</sup>. The high equilibrium carrier density means that meta-stable amorphous oxide semiconductors with lower carrier density for TFT channel application tend to have higher carrier density in the absence of kinetic constraints. For instance, if a post-deposition annealing

process at 200 °C is utilized, the carrier density of IAZO tends to reach the equilibrium carrier density of  $4.6 \times 10^{20} / \text{cm}^3$ . The required activation energy for carrier generation/annihilation of IAZO ( $E_a=0.81 \text{ eV}$ ) is slightly higher than that of IZO ( $E_a=0.73 \text{ eV}$ ), which may be due to the higher binding energy between the added third cation Al and oxygen (5.32 eV), compared to other binding energies of In-O (3.74 eV) and Zn-O (2.95 eV) <sup>44-47</sup>.

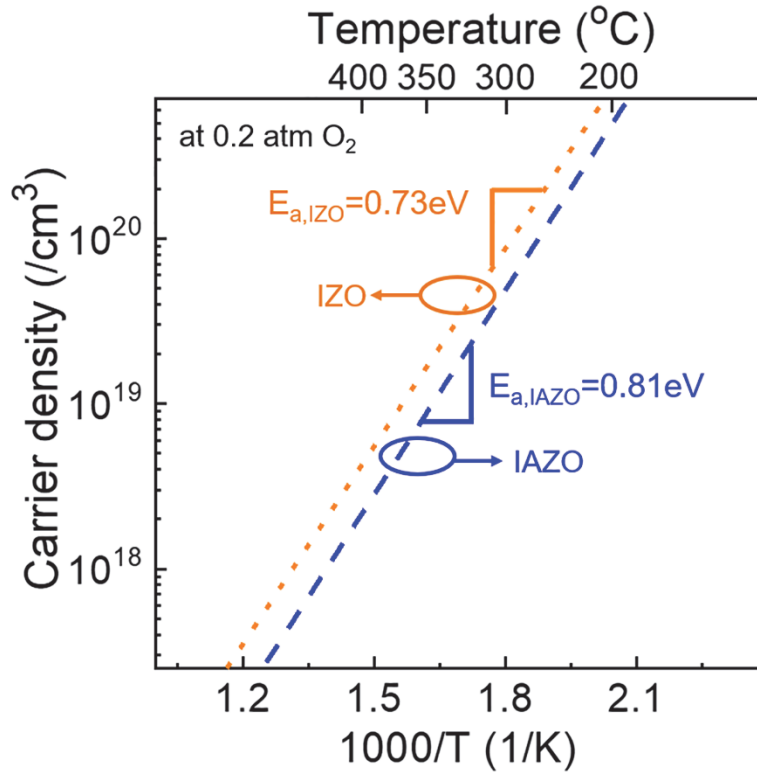


**Figure 6.** Equilibrium carrier density estimation of amorphous IAZO on an Arrhenius plot with the activation energy of carrier generation/annihilation of 0.81 eV, where the equilibrium carrier density at 200 °C is much higher than those typically used for TFT channel application,  $\sim 10^{14}$ - $10^{18} / \text{cm}^3$ . The equilibrium carrier density of a binary cation AOS of IZO is also plotted for comparison with the activation energy of 0.73 eV.

In  $\text{In}_2\text{O}_3$ -based amorphous oxide semiconductors such as IZO and IGZO, and IAZO in this study, defect states within the bandgap are mainly governed by oxygen vacancies, particularly for doping-related states. Depending on the valence states of oxygen vacancies, these defects states can form as either deep level or shallow level states, where the latter is located near the

conduction band and effective to donate free electrons, while the former is typically located near the valence band and not activated to contribute to doping. Some studies reported that changes in carrier density and hence conductivity after annealing were mainly attributed to the oxygen vacancy-based carrier generation/annihilation mechanism. Bae *et al.*<sup>48</sup> and Lee *et al.*<sup>49</sup> related that annealing in oxygen deficient conditions (e.g., N<sub>2</sub> or vacuum) led to an increase in carrier density of IGZO, and Park *et al.*<sup>50</sup> reported a similar result on InZrZnO, possibly due to the generation of oxygen vacancies from the desorption of surface oxygens (e.g., M-OH)<sup>49, 51</sup>. By the same mechanism, Hosono *et al.*<sup>21-22</sup> reported that annealing in air or other O<sub>2</sub> conditions decreased the free carrier density in IGZO due to the annihilation of oxygen vacancies.

However, as observed in the current report, studies are also found in the literature that show an increase in carrier density after annealing in the presence of O<sub>2</sub>, for which the oxygen-vacancy mechanism is not responsible for the carrier density increase. Fortunato *et al.*<sup>20, 52</sup> reported that the carrier density of IZO and AlZnO increased after annealing with O<sub>2</sub>, which consequently led to a negative shift in threshold voltage and high off-currents in TFT application. More recently, an approach of high pressure oxidation annealing has been demonstrated for IGZO by Kim *et al.*<sup>53</sup> to limit annealing temperatures up to 100 °C, which is available due to the enhanced reactivity of oxygen at elevated pressures (>1 MPa). The high pressure annealing resulted in more reliable IGZO TFT performance likely due to the stabilization of metal cation and oxygen bonds in IGZO. It should be noted that the carrier concentration of the IGZO annealed through high pressure oxidation is higher than that annealed with N<sub>2</sub>. They attributed the increase in carrier density after O<sub>2</sub> annealing to the enhanced kinetic energy of O<sub>2</sub> at high pressures, which aids IGZO to reach a more stable state with equilibrium carrier density. These studies that report

an increase in carrier density after annealing in air or O<sub>2</sub> conditions support our findings of an unusual increase in channel carrier density after air-annealing with enhanced TFT performance.

The high pressure oxidation investigation on the equilibrium carrier density for IAZO is further supported by a mechanism suggesting energy state transitions within the bandgap. Previous studies are found in the literature that report that a post-annealing process leads to a structural relaxation in IGZO and drives a defect state transition from deep level energy states to shallow level states. Through modeling studies based on density functional theory, Kamiya *et al.* demonstrated that a post-annealing process at 400 °C provides energies to activate neutrally charged oxygen vacancies (i.e., V<sub>O</sub>), which are initially positioned at deep level states (i.e., near the valence band) and shift toward the conduction band after annealing<sup>23-24</sup>. Yeon *et al.* experimentally proved the defect state transition from deep levels to shallow levels from current-voltage measurements of IGZO-based Schottky diode after annealing at 400 °C in air for 1-16 hours<sup>25</sup>. The increase in carrier density of IAZO after annealing, explored in this study, is analogous to that observed in IGZO, in the context of carrier density increment without changes in oxygen vacancy concentration. The finding from this study – non-equilibrium carrier density of IAZO in the metastable amorphous state tends to increase provided with thermal energies to reach the equilibrium carrier concentration, in the absence of kinetic constraints – can be further understood by the defect state transition mechanism. Un-activated oxygen vacancies (neutrally charged) in IAZO may be positioned near the valence band as shallow states in the as-deposited state. Some portion of the un-activated vacancies (approximately 0.22% based on the estimation of  $\Delta n_{\text{anneal}}/\Delta n_{\text{equilibrium}} = \sim 10^4/4.6 \times 10^6$  from the as-deposited concentration  $\sim 10^{14} / \text{cm}^3$ , the annealed concentration  $\sim 10^{18} / \text{cm}^3$ , and the equilibrium concentration  $4.6 \times 10^{20} / \text{cm}^3$ ) is likely to

be activated after annealing at 200 °C for 1 hour and these states are located near the conduction band as shallow level states. It should be noted, however, that the annealing temperature of 200 °C for IAZO TFTs used in this study is much lower than 400 °C used for IGZO devices in the previous reports<sup>23-25</sup>. In addition, the required activation energy (0.73 eV) for the structural relaxation in IAZO is smaller than 1.76 eV of IGZO<sup>25</sup>, indicating that the location of defect states of IAZO within the gap is higher than those of IGZO (deep level states of IGZO closer to the valence band when the bandgap of IAZO and IGZO are similar to each other as 3.2-3.3 eV vs ~3.2 eV<sup>24</sup>, respectively).

#### **4. Conclusions**

High field effect mobility (~22 cm<sup>2</sup>/Vs) and low threshold voltage (~-1.8 V) were obtained for ternary cation-based AOS TFT devices after low temperature annealing at 200 °C, compared to the as-deposited counterparts of ~7 cm<sup>2</sup>/Vs and 7.5 V. Work function investigations identified an abrupt increase (> 10<sup>4</sup> times) in channel IAZO carrier density. The typical intrinsic doping mechanism for indium oxide-based AOS based on native-based doping and a possible extrinsic doping based on cation substitution are found not to be the primary cause of the large increase in carrier density after low temperature annealing. Equilibrium carrier density calculations reveal that the equilibrium carrier density of IAZO at 200 °C is considerably higher (~4.6×10<sup>20</sup> /cm<sup>3</sup>) than those typically considered in TFT channel application, ~10<sup>14</sup>-10<sup>18</sup> /cm<sup>3</sup>. The high equilibrium carrier density indicates that in the absence of kinetic constraints, the channel carrier density tends to increase to reach equilibrium concentrations. This study may provide the important scientific prediction for AOS TFTs that show changes in channel carrier density and the associated device parameters such as threshold voltage.

## **Acknowledgements**

The authors gratefully acknowledge the financial support of the U.S. National Science Foundation (NSF) Award No. ECCS-1931088. SL thanks the support from Purdue University, the Purdue Research Foundation (Grant No. 60000029) and the Polytechnic RDE SEED program. KN is supported by Basic Science Research Program (NRF-2018R1A2B6002194) through the NRF Korea funded by the Ministry of Science and ICT. HWS & SL acknowledges the support from the Improvement of Measurement Standards and Technology for Mechanical Metrology (Grant No. 20011028) by KRISS.

## References

1. Nomura, K.; Ohta, H.; Takagi, A.; Kamiya, T.; Hirano, M.; Hosono, H., Room-temperature fabrication of transparent flexible thin-film transistors using amorphous oxide semiconductors. *Nature* **2004**, *432* (7016), 488-492.
2. Lee, S.; Paine, D. C., Metallization selection and the performance of amorphous In-Zn-O thin film transistors. *Applied Physics Letters* **2014**, *104* (25), 252103.
3. Fortunato, E.; Ginley, D.; Hosono, H.; Paine, D. C., Transparent conducting oxides for photovoltaics. *MRS Bull.* **2007**, *32* (3), 242-247.
4. Venkatanarayanan, A.; Spain, E., 13.03 - Review of Recent Developments in Sensing Materials. In *Comprehensive Materials Processing*, Hashmi, S.; Batalha, G. F.; Van Tyne, C. J.; Yilbas, B., Eds. Elsevier: Oxford, 2014; pp 47-101.
5. Zhao, S.; Choi, D.; Lee, T.; Boyd, A. K.; Barbara, P.; Van Keuren, E.; Hahm, J.-i., Indium Tin Oxide Nanowire Networks as Effective UV/Vis Photodetection Platforms. *The Journal of Physical Chemistry C* **2015**, *119* (26), 14483-14489.
6. Yeom, H. Y.; Popovich, N.; Chason, E.; Paine, D. C., A study of the effect of process oxygen on stress evolution in d.c. magnetron-deposited tin-doped indium oxide. *Thin Solid Films* **2002**, *411* (1), 17-22.
7. Drewelow, G.; Reed, A.; Stone, C.; Roh, K.; Jiang, Z.-T.; Truc, L. N. T.; No, K.; Park, H.; Lee, S., Work function investigations of Al-doped ZnO for band-alignment in electronic and optoelectronic applications. *Applied Surface Science* **2019**, *484*, 990-998.
8. Freeman, A. J.; Poepelmeier, K. R.; Mason, T. O.; Chang, R. P. H.; Marks, T. J., Chemical and thin-film strategies for new transparent conducting oxides. *MRS Bull.* **2000**, *25* (8), 45-51.
9. Hosono, H.; Yasukawa, M.; Kawazoe, H., Novel oxide amorphous semiconductors: transparent conducting amorphous oxides. *Journal of Non-Crystalline Solids* **1996**, *203*, 334-344.
10. Lee, S.; Park, K.; Paine, D. C., Metallization strategies for In<sub>2</sub>O<sub>3</sub>-based amorphous oxide semiconductor materials. *Journal of Materials Research* **2012**, *27* (17), 2299-2308.
11. Lee, S.; Park, H.; Paine, D. C., A study of the specific contact resistance and channel resistivity of amorphous IZO thin film transistors with IZO source-drain metallization. *Journal of Applied Physics* **2011**, *109* (6), 063702.
12. Reed, A.; Stone, C.; Roh, K.; Song, H. W.; Wang, X.; Liu, M.; Ko, D.-K.; No, K.; Lee, S., The role of third cation doping on phase stability, carrier transport and carrier suppression in amorphous oxide semiconductors. *Journal of Materials Chemistry C* **2020**, *8* (39), 13798-13810.
13. Nomura, K.; Kamiya, T.; Hirano, M.; Hosono, H., Origins of threshold voltage shifts in room-temperature deposited and annealed a-In-Ga-Zn-O thin-film transistors. *Applied Physics Letters* **2009**, *95* (1), 013502.
14. Lee, S.; Bierig, B.; Paine, D. C., Amorphous structure and electrical performance of low-temperature annealed amorphous indium zinc oxide transparent thin film transistors. *Thin Solid Films* **2012**, *520* (10), 3764-3768.
15. Shimura, Y.; Nomura, K.; Yanagi, H.; Kamiya, T.; Hirano, M.; Hosono, H., Specific contact resistances between amorphous oxide semiconductor In-Ga-Zn-O and metallic electrodes. *Thin Solid Films* **2008**, *516* (17), 5899-5902.
16. Ide, K.; Nomura, K.; Hosono, H.; Kamiya, T., Electronic Defects in Amorphous Oxide Semiconductors: A Review. *physica status solidi (a)* **2019**, *216* (5), 1800372.
17. Liu, J.; Buchholz, D. B.; Hennek, J. W.; Chang, R. P. H.; Facchetti, A.; Marks, T. J., All-Amorphous-Oxide Transparent, Flexible Thin-Film Transistors. Efficacy of Bilayer Gate Dielectrics. *Journal of the American Chemical Society* **2010**, *132* (34), 11934-11942.

18. Nomura, K.; Kamiya, T.; Ohta, H.; Hirano, M.; Hosono, H., Defect passivation and homogenization of amorphous oxide thin-film transistor by wet O<sub>2</sub> annealing. *Applied Physics Letters* **2008**, *93* (19).
19. Kikuchi, Y.; Nomura, K.; Yanagi, H.; Kamiya, T.; Hirano, M.; Hosono, H., Device characteristics improvement of a-In-Ga-Zn-O TFTs by low-temperature annealing. *Thin Solid Films* **2010**, *518* (11), 3017-3021.
20. Barquinha, P.; Goncalves, G.; Pereira, L.; Martins, R.; Fortunato, E., Effect of annealing temperature on the properties of IZO films and IZO based transparent TFTs. *Thin Solid Films* **2007**, *515* (24), 8450-8454.
21. Nomura, K.; Kamiya, T.; Ohta, H.; Hirano, M.; Hosono, H., Defect passivation and homogenization of amorphous oxide thin-film transistor by wet O<sub>2</sub> annealing. *Applied Physics Letters* **2008**, *93* (19), 192107.
22. Ide, K.; Kikuchi, Y.; Nomura, K.; Kamiya, T.; Hosono, H., Effects of low-temperature ozone annealing on operation characteristics of amorphous In-Ga-Zn-O thin-film transistors. *Thin Solid Films* **2012**, *520* (10), 3787-3790.
23. Kamiya, T.; Nomura, K.; Hirano, M.; Hosono, H., Electronic structure of oxygen deficient amorphous oxide semiconductor a-InGaZnO<sub>4-x</sub> : Optical analyses and first-principle calculations. *physica status solidi c* **2008**, *5* (9), 3098-3100.
24. Kamiya, T.; Nomura, K.; Hosono, H., Electronic structure of the amorphous oxide semiconductor a-InGaZnO<sub>4-x</sub> : Tauc-Lorentz optical model and origins of subgap states. *physica status solidi (a)* **2009**, *206* (5), 860-867.
25. Yeon, H.-W.; Lim, S.-M.; Jung, J.-K.; Yoo, H.; Lee, Y.-J.; Kang, H.-Y.; Park, Y.-J.; Kim, M.; Joo, Y.-C., Structural-relaxation-driven electron doping of amorphous oxide semiconductors by increasing the concentration of oxygen vacancies in shallow-donor states. *NPG Asia Materials* **2016**, *8* (3), e250-e250.
26. Caragianis, C.; Shigesato, Y.; Paine, D. C., High Pressure Oxidation for Low Temperature Passivation of Si<sub>1-x</sub>Gex Alloys. In *The Physics and Chemistry of SiO<sub>2</sub> and the Si-SiO<sub>2</sub> Interface 2*, Helms, C. R.; Deal, B. E., Eds. Springer US: Boston, MA, 1993; pp 71-79.
27. Paine, D. C.; Caragianis, C.; Schwartzman, A. F., Oxidation of Si<sub>1-x</sub>Gex alloys at atmospheric and elevated pressure. *Journal of Applied Physics* **1991**, *70* (9), 5076-5084.
28. Takagi, A.; Nomura, K.; Ohta, H.; Yanagi, H.; Kamiya, T.; Hirano, M.; Hosono, H., Carrier transport and electronic structure in amorphous oxide semiconductor, a-InGaZnO<sub>4</sub>. *Thin Solid Films* **2005**, *486* (1-2), 38-41.
29. Paine, D. C.; Yaglioglu, B.; Beiley, Z.; Lee, S., Amorphous IZO-based transparent thin film transistors. *Thin Solid Films* **2008**, *516* (17), 5894-5898.
30. Reed, A. S.; Paine, D. C.; Lee, S., Effect of O<sub>2</sub> Fraction in the Sputter Gas on the Electrical Properties of Amorphous In-Zn-O and the Thin Film Transistor Performance. *Journal of Electronic Materials* **2016**, *45* (12), 6310-6316.
31. Kamiya, T.; Nomura, K.; Hosono, H., Present status of amorphous In-Ga-Zn-O thin-film transistors. *Science and Technology of Advanced Materials* **2010**, *11* (4), 044305.
32. Leenheer, A. J.; Perkins, J. D.; van Hest, M. F. A. M.; Berry, J. J.; O'Hayre, R. P.; Ginley, D. S., General mobility and carrier concentration relationship in transparent amorphous indium zinc oxide films. *Physical Review B* **2008**, *77* (11), 115215.
33. Hirose, Y.; Yamada, N.; Nakao, S.; Hitosugi, T.; Shimada, T.; Hasegawa, T., Large electron mass anisotropy in a d<sup>0</sup>-electron-based transparent conducting oxide: Nb-doped anatase TiO<sub>2</sub> epitaxial films. *Physical Review B* **2009**, *79* (16), 165108.
34. Jia, J. J.; Oka, N.; Shigesato, Y., Direct observation of the band gap shrinkage in amorphous In<sub>2</sub>O<sub>3</sub>-ZnO thin films. *Journal of Applied Physics* **2013**, *113* (16), 163702.

35. Jeong, S.; Ha, Y.-G.; Moon, J.; Facchetti, A.; Marks, T. J., Role of Gallium Doping in Dramatically Lowering Amorphous-Oxide Processing Temperatures for Solution-Derived Indium Zinc Oxide Thin-Film Transistors. *Adv. Mater.* **2010**, *22* (12), 1346-1350.
36. Donley, C.; Dunphy, D.; Paine, D.; Carter, C.; Nebesny, K.; Lee, P.; Alloway, D.; Armstrong, N. R., Characterization of Indium–Tin Oxide Interfaces Using X-ray Photoelectron Spectroscopy and Redox Processes of a Chemisorbed Probe Molecule: Effect of Surface Pretreatment Conditions. *Langmuir* **2002**, *18* (2), 450-457.
37. Lee, S.; Paine, D. C., Identification of the native defect doping mechanism in amorphous indium zinc oxide thin films studied using ultra high pressure oxidation. *Applied Physics Letters* **2013**, *102* (5), 052101.
38. Jia, J.; Suko, A.; Shigesato, Y.; Okajima, T.; Inoue, K.; Hosomi, H., Evolution of Defect Structures and Deep Subgap States during Annealing of Amorphous In-Ga-Zn Oxide for Thin-Film Transistors. *Physical Review Applied* **2018**, *9* (1), 014018.
39. Limpijumnong, S.; Reunchan, P.; Janotti, A.; Van de Walle, C. G., Hydrogen doping in indium oxide: An ab initio study. *Phys. Rev. B* **2009**, *80* (19), 193202.
40. Reunchan, P.; Zhou, X.; Limpijumnong, S.; Janotti, A.; Van de Walle, C. G., Vacancy defects in indium oxide: An ab-initio study. *Curr Appl Phys* **2011**, *11* (3), S296-S300.
41. Thomas, D. G., Infrared absorption in zinc oxide crystals. *Journal of Physics and Chemistry of Solids* **1959**, *10* (1), 47-51.
42. Ellmer, K., *Transparent Conductive Zinc Oxide and Its Derivatives*. 2010; p 193-263.
43. Lee, S.; Paine, D. C., On the effect of Ti on the stability of amorphous indium zinc oxide used in thin film transistor applications. *Applied Physics Letters* **2011**, *98* (26), 262108.
44. Cottrell, T. L., *The Strengths of Chemical Bonds*. Butterworth: 1961.
45. Darwent, B. B., *Bond Dissociation Energies in Simple Molecules*. U.S. National Bureau of Standards: 1970.
46. Benson, S. W., III - Bond energies. *Journal of Chemical Education* **1965**, *42* (9), 502.
47. Kerr, J. A., Bond Dissociation Energies by Kinetic Methods. *Chemical Reviews* **1966**, *66* (5), 465-500.
48. Bae, H.-s.; Kwon, J.-H.; Chang, S.; Chung, M.-H.; Oh, T.-Y.; Park, J.-H.; Lee, S. Y.; Pak, J. J.; Ju, B.-K., The effect of annealing on amorphous indium gallium zinc oxide thin film transistors. *Thin Solid Films* **2010**, *518* (22), 6325-6329.
49. Lee, H.-W.; Cho, W.-J., Effects of vacuum rapid thermal annealing on the electrical characteristics of amorphous indium gallium zinc oxide thin films. *AIP Advances* **2018**, *8* (1), 015007.
50. Park, J.-S.; Kim, K.; Park, Y.-G.; Mo, Y.-G.; Kim, H. D.; Jeong, J. K., Novel ZrInZnO Thin-film Transistor with Excellent Stability. *Adv. Mater.* **2009**, *21* (3), 329-333.
51. Fuh, C.-S.; Sze, S. M.; Liu, P.-T.; Teng, L.-F.; Chou, Y.-T., Role of environmental and annealing conditions on the passivation-free in-Ga–Zn–O TFT. *Thin Solid Films* **2011**, *520* (5), 1489-1494.
52. Lyubchik, A.; Vicente, A.; Soule, B.; Alves, P. U.; Mateus, T.; Mendes, M. J.; Águas, H.; Fortunato, E.; Martins, R., Mapping the Electrical Properties of ZnO-Based Transparent Conductive Oxides Grown at Room Temperature and Improved by Controlled Postdeposition Annealing. *Advanced Electronic Materials* **2016**, *2* (1), 1500287.
53. Kim, W.-G.; Tak, Y. J.; Du Ahn, B.; Jung, T. S.; Chung, K.-B.; Kim, H. J., High-pressure Gas Activation for Amorphous Indium–Gallium–Zinc–Oxide Thin-Film Transistors at 100 °C. *Scientific Reports* **2016**, *6* (1), 23039.